Journal of Materials Chemistry A

Long-Term Stability Studies of a Semiconductor Photoelectrode Protected by Gallium Nitride Nanostructures

Journal:	*Journal of Materials Chemistry A*
Manuscript ID	TA-ART-09-2019-009926.R1
Article Type:	Paper
Date Submitted by the Author:	13-Nov-2019
Complete List of Authors:	Vanka, Srinivas; University of Michigan, Electrical Engineering & Computer Science; McGill University Sun, Kai; University of Michigan, Materials Science and Engineering Zeng, Guosong; Lawrence Berkeley National Laboratory, Chemical Sciences Division Pham, Tuan; Lawrence Livermore National Laboratory, Quantum Simulations Group Toma, Francesca Maria; Lawrence Berkeley National Lab, Chemical Sciences Division Ogitsu, Tadashi; Lawrence Livermore National Laboratory, Quantum Simulations Group Mi, Zetian; University of Michigan, Electrical Engineering & Computer Science

SCHOLARONE™
Manuscripts

Long-Term Stability Studies of a Semiconductor Photoelectrode Protected by Gallium Nitride Nanostructures

Srinivas Vanka[1,2], Kai Sun[3], Guosong Zeng[4], Tuan Anh Pham[5], Francesca Maria Toma[4], Tadashi Ogitsu[5] and Zetian Mi[1*]

[1] *Department of Electrical Engineering and Computer Science, University of Michigan, Ann Arbor, 1301 Beal Avenue, Ann Arbor, MI 48109, USA*

[2] *Department of Electrical and Computer Engineering, McGill University, 3480 University Street, Montreal, Quebec, H3A 0E9, Canada*

[3] *Department of Materials Science and Engineering, University of Michigan, 2300 Hayward Street, Ann Arbor, MI 48109, USA*

[4] *Lawrence Berkeley National Laboratory, Chemical Sciences Division, 1 Cyclotron Road, Berkeley, CA 94720, USA*

[5] *Lawrence Livermore National Laboratory, Quantum Simulations Group, 7000 East Avenue, L-413, Livermore, CA 94550, USA*

[*] *Corresponding author E-mail: ztmi@umich.edu; Phone: +1 734 764 3963*

Abstract

Improving the stability of semiconductor materials is one of the major challenges for sustainable and economic photoelectrochemical water splitting. N-terminated GaN nanostructures have emerged as a practical protection layer for conventional high efficiency but unstable Si and III-V photoelectrodes, due to their near-perfect conduction band-alignment, which enables efficient extraction of photo-generated electrons, and N-terminated surfaces, which protects against chemical and photo-corrosion. Here, we demonstrate that Pt-decorated GaN nanostructures on n^+-*p* Si photocathode can exhibit ultrahigh stability of 3000 h (*i.e.,* over 500 days for usable sunlight ~5.5 h per day) at a large photocurrent density (> 35 mA/cm^2) under AM 1.5G one-sun illumination. The measured applied bias photon-to-current efficiency of 11.9%, with an excellent onset potential of ~ 0.56 V *vs.* RHE, is one of the highest values reported for a Si photocathode under AM 1.5G one-sun illumination. This study provides a paradigm shift for the design and development of semiconductor photoelectrodes for PEC water splitting: stability is no longer limited by the light absorber, but rather by co-catalyst particles.

Introduction

Photoelectrochemical (PEC) solar water splitting is one of the clean and sustainable approaches to convert the two most abundant natural resources on earth, *i.e.,* sunlight and water, into high calorific value, storable and clean chemical fuels such as hydrogen (H_2) [1-6]. It is essential to develop high efficiency, durable, and cost-effective photoelectrode materials using industry-ready semiconductors for large-scale implementation of PEC devices [5, 7, 8]. To date, high efficiency photoelectrodes have been demonstrated using only a few semiconductors, including Si [6, 9-13] and III-V compound semiconductors [14-18], which, however, suffer from poor stability due to chemical and photochemical corrosion [19-22]. Compared to photovoltaic electrolyser (PV-EL) devices, the light absorber of PEC devices is often in direct contact with electrolyte [23], leading to more rapid degradation. The corrosion of semiconductors is influenced by many factors, including intensity of light illumination, biasing conditions, catalyst, surface passivation, semiconductor electronic band structure, electrolyte composition, and the interfaces of semiconductor/electrolyte as well as catalyst/electrolyte [6, 19, 20, 24]. These factors can be potentially addressed by exploring thermodynamic and kinetic protection schemes.

Gerischer's model [25] describes the thermodynamic considerations for photo-corrosion of a photoelectrode. To avoid competition between cathodic and anodic photo-corrosion of photoelectrode with hydrogen evolution reaction (HER) and oxygen evolution reaction (OER), respectively, it is vital that the photoelectrodes satisfy the basic criteria: $\phi_{corr}^{h} < E_{anodic}$ (1.23 V *vs.* RHE) and $\phi_{corr}^{e} > E_{cathodic}$ (0 V *vs.* RHE), where ϕ_{corr}^{e} is energy level for cathodic corrosion reaction of semiconductor, and ϕ_{corr}^{h} is energy level for anodic corrosion reaction of semiconductor. Previous studies [26, 27] have shown that it is difficult to find an ideal semiconductor material that can satisfy both thermodynamic requirements simultaneously. Si can be easily

oxidized under anodic conditions but is expected to be thermodynamically stable under cathodic conditions [26]. Other studies, however, suggested that Si could also get oxidized into an insulating oxide even under cathodic conditions [24, 28], which leads to poor stability. III-V compounds, such as GaAs, often go through chemical corrosion reaction due to accumulation of surface hole concentration in dark and light [29]. In this regard, various protection schemes have been developed to enhance the stability of photoelectrodes [20]. Kinetic protection for a given photoelectrode is possible by using a synergetic combination of stable surface protection layer and highly active co-catalyst [19, 20]. The first generation of photoelectrodes often rely on the coupling with highly active catalysts, illustrated in Figure 1(a), which can improve the stability due to the excellent reaction kinetics and more efficient charge carrier extraction. Recent studies showed that hematite (α-Fe_2O_3) and bismuth vanadate ($BiVO_4$) with NiFe co-catalyst exhibited a high level of stability with efficiencies reaching their theoretical maximum values [30,31]. Extensive studies have also been performed with the use of Pt [32-35], MoS_2 [11, 15, 16, 36, 37] and NiMo [38, 39] as both protection layers and co-catalysts for HER. To further improve the device stability, the second generation of photoelectrodes, illustrated in Figure 1(b), employ relatively thick metal oxides, such as TiO_2 [27, 40-42], Al_2O_3 [43], and IrO_x [44], as passivation layers, in addition to the use of suitable co-catalysts [27, 44-46]. Although the stability of these devices has improved, one major issue is the loss of photocurrent, due to poor charge transfer and, in some cases, undesired light absorption of the protection layers [19, 21, 47]. One of the best-performing photocathodes, in terms of stability, was reported by Bae *et al.* [23] using Pt co-catalyst and 100 nm thick TiO_2 for metal oxide semiconductor junctions Si photocathode, which exhibits stable operation for ~82 days with a photocurrent density ($\leq$ 23 mA/cm^2) (see Table S1, ESI).

In this context, we envision that, to achieve both high efficiency and long-term stability, a multi-functional surface protection scheme should be developed, schematically shown in Figure 1(c). Such a protection scheme should offer not only robust surface protection but also significantly improved optical, electrical, and photoelectrochemical performance. In this study, we demonstrate such a unique class of photoelectrodes by integrating Pt-decorated N-rich GaN nanostructures with n^+-p Si wafer. The N-terminated surfaces of GaN can protect the underlying Si absorber against photocorrosion and oxidation[48-50]. Unique to the GaN/Si heterointerface is that the conduction band edges are near-perfectly aligned, thereby leading to efficient extraction of photo-generated charge carriers (electrons) from the undelying Si absorber, schematically shown in Figure 1(d). In this work we demonstrate that, with such a unique surface protection scheme, Si photocathodes can exhibit an ultrahigh stability of 3,000 h with a stable photocurrent density ~38 mA/cm^2 in 0.5 M H_2SO_4 under AM 1.5 G one sun illumination, which, to the best of our knowledge, is the longest stability ever measured for any photoelectrode materials for H_2 production in a half-cell configuration (see Table S1, ESI). The best performing platinized n^+-GaN nanowires/n^+-p Si photocathode showed excellent onset potential (V_{on}) ~0.56 V *vs.* RHE with high photocurrent density of ~37 mA/cm^2 and a high applied bias photon-to-current efficiency (ABPE) of 11.9%. The device stability is further studied by using atomic force microscopy (AFM) measurements. Significantly, the utilization of GaN and Si, two most produced semiconductor materials in the world, to realize high efficiency and highly stable photoelectrochemical water splitting provides a scalable and practical approach for solar fuel production.

Results and discussion

In this study, n^+-GaN nanowires were grown on n^+-p Si wafer using a Veeco GEN II molecular beam epitaxial (MBE) system equipped with a radio frequency plasma-assisted nitrogen source (see Experimental section, ESI). The fabrication of n^+-p Si substrate was discussed in previous reports [9]. Illustrated in Figure 1(d), the conduction band minimum (CBM) for n^+-GaN is near-perfectly aligned with that of n^+-Si [9], which was measured using XPS in previous studies [9]. Consequently, photo-generated electrons from n^+-p Si substrate can be efficiently extracted by GaN nanowires, *i.e.,* with negligible resistivity, even when a relatively thick GaN protection layer is employed (see Figure S2, ESI), which is in direct contrast to the undesirable high resistivity associated with a relatively thick conventional protection scheme [9, 11, 41, 51]. Shown in Figure 2(a) is the scanning electron microscope (SEM) image of as grown nanowires, which are vertically aligned to the Si substrate, with an average length ~400 nm and diameter ~40 nm. A detailed description of the photoelectrode preparation, including photo-deposition of Pt nanoparticles is presented in Experimental section, ESI. The structural characterization after Pt photo-deposition for the samples was performed using scanning transmission electron microscopy (STEM). Figure 2(b) shows the distribution of Pt nanoparticles around GaN nanowires. In Figure S1, ESI, further STEM images are illustrated for GaN nanowires after Pt deposition. Figure 2(c) shows the linear scan voltammogram (LSV) of Pt-decorated n^+-GaN nanowires on n^+-p Si photocathode under AM 1.5G one sun illumination (red curve) and dark (black curve) conditions. The Pt/n^+-GaN nanowires/n^+-p Si photocathode showed excellent performance with an onset potential (V_{on}) of ~0.56 V *vs* RHE and high photocurrent density of ~37 mA/cm^2 under AM 1.5G one-sun illumination in 0.5 M H_2SO_4. Shown in Figure 2(d), the maximum ABPE (see Experimental section, ESI) for Pt/n^+-GaN nanowires/n^+-p Si photocathode (red curve) is 11.9% at 0.38 V *vs.*

RHE under AM 1.5G one sun illumination, which is one of the best reported values for Si photocathodes [9, 13, 41, 52]. For the stability tests (both under dark and light), we have chosen samples with ABPE ≥ 10% and J at 0 V *vs.* RHE ~38 mA/cm^2.

Before starting the stability experiments, the electrode was thoroughly rinsed with distilled water and dried with N_2 gun. The photoelectrode was then placed in 0.5 M H_2SO_4 inside the PEC chamber, and the stability experiment was conducted at a constant applied potential of 0 V *vs.* RHE under AM1.5G one-sun illumination. Our initial studies, as described in previous reports, showed that stability ~113 h can be achieved. Further stability testing, however, showed performance degradation (see Figure S3(a), ESI). In Figure S3(b), ESI, STEM image shows considerable loss of Pt nanoparticles on GaN nanowire surface, which explains the poor onset potential. The photoelectrode material itself, including GaN and Si, showed no sign of degradation. To study the intrinsic stability of GaN/Si photocathodes, in this work we have therefore employed the catalyst regeneration process, which was performed after approximately every 24 h PEC experiments (see Experimental section, ESI). The entire process is schematically shown in Scheme S1, ESI. After each catalyst regeneration, the *J-V* characteristics were measured under both dark and AM 1.5G one-sun illumination and were compared to the 0th h *J-V* characteristics (Figures S4(a), (b) and (c), ESI). Then the experiment was resumed for the next cycle of stability test and catalyst regeneration. The details of each regeneration cycle are summarized in Table S2, ESI. It is important to mention here that after every 24 h experiment, the electrolyte was replaced with a fresh solution to maintain a constant pH ~0 for all the runs and to reduce possible carbonaceous contaminations from epoxy [23].

Figure 3(a) shows the photocurrent density variation over the entire duration of 3,000 h for Pt/n^+-GaN nanowires/n^+-p Si photocathode under AM 1.5G one-sun illumination at 0 V *vs.* RHE

in 0.5 M H_2SO_4. Shown in Figure 3(b), for 80-264 h runs, *i.e.,* between the 4th and 12th regeneration cycles (see Table S2, ESI), the photocurrent density varied between 36-40 mA/cm^2, which is within ±10% of the average J_0 value measured at 0 V *vs.* RHE. Figure 3(c) shows that the variations in J increased to ~±20-25% from 1270 to 1539 h, *i.e.,* between 59 and 73 regeneration cycles (see Table S2, ESI). These variations are mainly due to the unexpected epoxy meltdown, malfunctioning of potentiostat (due to electrical fluctuations in the building) and poor backside contact. In these cases, we had to stop the experiments and troubleshoot these issues, which lead to increase in the number of regeneration cycles as shown in Table S2, ESI. The experimental problems were addressed during the subsequent runs by frequently redoing the backside contact after every 100-120 h runs and carefully monitoring the potentiostat during the cycles. Figure 3(d) shows that the photocurrent variations for 2350-2640 h runs (between the 113th and 125th regeneration cycles) is within ±10% of the J_0. It is to be noted that despite photocurrent variations, the *J-V* characteristics at the start of the 141st regeneration cycle, *i.e.,* after 3008 h run with Pt redeposition, are nearly the same as the J_0 curve at the start of the experiments (see Figure 3(e) and Figure S4(d), ESI), which implies that GaN nanowires remain intact on Si surface. Furthermore, Figure 3(f) shows the variation of V_{on} for each regeneration cycle at the start (purple curve) and end (red curve) of each cycle. The slight reduction of V_{on} at the end of each regeneration cycle is due to the loss of some Pt nanoparticles as described earlier. The catalyst regeneration, at the start of each cycle, helps in immediately recovering the V_{on} for the LSV curves (see Figure S4(d), ESI).

Detailed structural characterization was further performed after 3,000 h experiments. SEM image in Figure 4(a) shows that there is virtually no change in nanowire morphology compared to the as grown samples. Illustrated in Figure 4(b), STEM image shows that the nanowire length is

~400 nm and the diameter is ~ 40 nm, which are nearly identical to those shown in Figure 2(b). No apparent etching of the nanowire surface was observed. The inset in Figure 4(b) shows the reduction of Pt nanoparticles over the nanowire compared to Figure 2(b). More TEM images of the nanowires are shown in Figure S5, ESI. Due to the Pt nanoparticles falling-off, the *J-V* curve immediately at the end of the 140th regeneration cycle (see blue curve in Figure S4(c), ESI) degraded somewhat. By doing Pt regeneration at the start 141st regeneration cycle, the *J-V* characteristics were restored to the 0th h curves (see Figure S4(c), ESI), which clearly shows that GaN nanowires are still protecting the Si photocathode and the GaN-protected Si photocathode can last significantly longer than 3,000 h. The dark currents before and after Pt regenerations for the 46th, 96th, and 140th regeneration cycles (as shown in Figure S4, ESI and Table S2, ESI) are nearly the same as the 0th h dark current. In Figure S6, ESI, the ABPE for the 0th h and at the start of the 141st regeneration cycles under AM 1.5G one-sun illumination is found to be ~10%. These results are also consistent with the nearly identical X-ray diffraction measurements performed on the sample before and after stability test (see Figure S7, ESI). The dissolved Ga and Pt elements in the electrolyte are analyzed using inductively coupled plasma mass spectroscopy (ICP-MS). ICP-MS results for different runs (see Figure S8, ESI and Experimental section, ESI) show dissolved Ga concentrations of 15-20 nmol and Pt concentrations of 1-5 nmol, considering an error bar ~ 10% in the measurements. These results clearly show that GaN remains stable throughout the course of the stability test which agrees well with the above-mentioned STEM analysis.

We also evaluated the Faraday efficiency (see Experimental section, ESI) by analyzing the H_2 generation from Pt/n^+-GaN nanowires/n^+-p Si photocathode between 0-2 h and 3000-3002 h. As shown in Figure 5(a), the photocurrent and H_2 evolution are simultaneously measured for the sample between 0-2 h at 0 V *vs.* RHE for a duration of 2 h in 0.5M H_2SO_4 under AM 1.5G one sun

illumination. Similarly, H_2 evolution experiment was carried out for the sample between 3000-3002 h (shown in Figure 5(b)) under the same conditions. In both cases, the Faraday efficiency is nearly 100%, considering that there is an error bar ~10% of H_2 sampling. Given the nearly identical LSV curves measured at 0 h and 3000 h, it is reasonably concluded that the GaN/Si photocathode can drive solar water splitting with stability over 3,000 h.

The total charge passed during 3000 h light experiment for Pt/n^+-GaN nanowires/n^+-p Si photocathode is 410,400 C/cm^2 by considering an average saturation photocurrent density of ~38 mA/cm^2 for 3,000 h. The presented platinized n^+-GaN nanowires/n^+-p Si photocathode for 3,000 h operation had the same amount of charge passed during >1.5 years of outdoor operation under AM 1.5G one-sun conditions with a solar capacity of 20% [5]. As the projected operation is a lower limit on the actual stability of Pt/n^+-GaN nanowires/n^+-p Si, it is required to do accelerated long-term stability tests with temperature and light intensity variations to precisely identify the degradation/corrosion mechanisms. Furthermore, Figure 5(c) shows the amount of H_2 production (in Lit/cm^2) at standard temperature and pressure (STP) conditions for some of the best reported long-term stability photocathodes [10, 11, 23, 42, 53] over the entire duration of the stability experiments. Compared to these photocathodes, the platinized n^+-GaN nanowires/n^+-p Si photocathode has the highest H_2 production of > 45 Lit/cm^2. These results, combined with the fact that GaN and Si are industry established materials, suggest the scalability and economic viability of this photocathode system for large-scale implementation of PEC water splitting. Recent studies show that the PEC characteristics for n^+-GaN nanowires/n^+-p Si photocathode are further improved by using controllable Pt loading amounts through PEC photo-deposition [51]. For future studies, we will focus on *in-situ* catalyst regeneration by using controllable Pt loading amounts, which can further reduce the H_2 production cost, to achieve ultrahigh stability and high efficiency.

We have also performed atomic force microscope (AFM) measurements on GaN-protected Si photocathodes before and after chronoamperometry testing to compare the morphology change due to the photoelectrochemistry. Since such AFM measurements can only be performed on planar surfaces, nearly coalesced GaN nanostructures with a quasi-planar morphology was used in this experiment. The measurement details are described in Experimental section, ESI. Shown in Figures 6(a) and (b), no change in surface morphology was observed for 10 h of reaction, further confirming that GaN is intrinsically stable in harsh photocatalysis conditions. Studies were also performed by varying the thickness of the GaN surface protection layer (see Figure S2, ESI). The measured photocurrent densities (shown in Figure S2, ESI) are nearly the same for the samples studied, which is consistent with the near-perfect conduction band alignment between GaN and Si measured previously.

The underlying mechanism for the unprecedentedly ultrahigh stability of GaN protected Si photocathode is described. Firstly, wurtzite GaN nanowires grown on Si wafer are nearly free of dislocations due to the efficient surface strain relaxation, and have strong ionic bonds which lead to bunching of surface states near the band edges [48, 54]. Our previous studies suggest that the presented GaN nanostructures have the unique N-termination, not only on the top c-plane surface but also for the lateral nonpolar surfaces, which can protect against photocorrosion and oxidation [48, 50]. As shown previously, there is also a thin GaN layer beneath the nanowires which protects the Si from the formation of insulating oxide and passivates the surface states to prevent charge carrier recombination [9]. Moreover, due to the negligibly small conduction band offset between Si and GaN there is virtually no loss in charge carrier extraction [9]. As such, the unique GaN nanostructures can protect the underlying Si surface against photo-corrosion with enhanced charge carrier extraction kinetics and better light absorption. The Pt/GaN interface further improves the

charge carrier extraction compared to Pt/Si [9, 51] and thereby enhances the overall stability of the photocathode. In future devices, the catalyst regeneration process can be minimized, or eliminated by utilizing more robust co-catalyst integration process, such as atomic layer integration.

Conclusion

In conclusion, we have demonstrated that Pt/n^+-GaN nanowires/n^+-p Si photocathode can exhibit both high efficiency and long-term stable operation. The unique GaN nanostructures can significantly enhance the performance of Si photocathodes (achieving high photocurrent density of ~ 38 mA/cm^2 and ABPE ~11.9%) and further provide extremely robust protection of the Si surface for over 3000 h (>500 days) without any performance degradation, *i.e.,* without any loss of photocurrent, onset potential, or efficiency. Future work includes a more fundamental understanding of the surface properties of such GaN nanostructures and the underlying mechanism for the extraordinary stability in harsh PEC water splitting. This unique PEC platform, by utilizing the two most produced semiconductors, *i.e.,* Si and GaN, lays a solid foundation for realizing practical PEC water splitting devices and systems that are efficient, stable, and of low cost.

Conflicts of interests. The authors declare no competing financial interests.

Acknowledgments

The authors gratefully acknowledge research support from the HydroGEN Advanced Water Splitting Materials Consortium, established as part of the Energy Materials Network under the U.S. Department of Energy, Office of Energy Efficiency and Renewable Energy, Fuel Cell Technologies Office, under Award Number DE-EE0008086, National Science Foundation under grant CBET 1804458, and Emissions Reduction Alberta. The authors acknowledge the financial

support of the University of Michigan College of Engineering and NSF grant #DMR-0723032, and technical support from the Michigan Center for Materials Characterization.

References

1. Y. He, T. Hamann and D. Wang, *Chem. Soc. Rev.*, 2019, DOI: 10.1039/c8cs00868j.
2. N. S. Lewis, *Science*, 2016, **351**, aad1920.
3. T. Lopes, P. Dias, L. Andrade and A. Mendes, *Sol. Energ. Mat. Sol. C*, 2014, **128**, 399-410.
4. M. Dumortier, S. Tembhurne and S. Haussener, *Energ. Environ. Sci.*, 2015, **8**, 3614-3628.
5. M. R. Shaner, H. A. Atwater, N. S. Lewis and E. W. McFarland, *Energ. Environ. Sci.*, 2016, **9**, 2354-2371.
6. R. Fan, Z. Mi and M. Shen, *Opt. Express*, 2019, **27**, A51.
7. B. A. Pinaud, J. D. Benck, L. C. Seitz, A. J. Forman, Z. Chen, T. G. Deutsch, B. D. James, K. N. Baum, G. N. Baum, S. Ardo, H. Wang, E. Miller and T. F. Jaramillo, *Energ. Environ. Sci.*, 2013, **6**, 1983.
8. S. Chu, W. Li, Y. Yan, T. Hamann, I. Shih, D. Wang and Z. Mi, *Nano Futures*, 2017, **1**, 022001.
9. S. Vanka, E. Arca, S. Cheng, K. Sun, G. A. Botton, G. Teeter and Z. Mi, *Nano Lett.*, 2018, **18**, 6530-6537.
10. B. Seger, D. S. Tilley, T. Pedersen, P. C. K. Vesborg, O. Hansen, M. Grätzel and I. Chorkendorff, *RSC Adv.*, 2013, **3**, 25902.
11. L. A. King, T. R. Hellstern, J. Park, R. Sinclair and T. F. Jaramillo, *ACS Appl. Mater. Interfaces*, 2017, **9**, 36792-36798.
12. J. D. Benck, S. C. Lee, K. D. Fong, J. Kibsgaard, R. Sinclair and T. F. Jaramillo, *Adv. Energ. Mater.*, 2014, **4**, 1400739.
13. H. P. Wang, K. Sun, S. Y. Noh, A. Kargar, M. L. Tsai, M. Y. Huang, D. L. Wang and J. H. He, *Nano Lett.*, 2015, **15**, 2817-2824.

14. D. Kang, J. L. Young, H. Lim, W. E. Klein, H. Chen, Y. Xi, B. Gai, T. G. Deutsch and J. Yoon, *Nat. Energ.*, 2017, **2**, 17043.
15. Q. Li, M. Zheng, M. Zhong, L. Ma, F. Wang, L. Ma and W. Shen, *Sci Rep*, 2016, **6**, 29738.
16. R. J. Britto, J. D. Benck, J. L. Young, C. Hahn, T. G. Deutsch and T. F. Jaramillo, *J. Phys. Chem. Lett.*, 2016, **7**, 2044-2049.
17. M. H. Lee, K. Takei, J. Zhang, R. Kapadia, M. Zheng, Y. Z. Chen, J. Nah, T. S. Matthews, Y. L. Chueh, J. W. Ager and A. Javey, *Angew. Chem. Int. Ed. Engl.*, 2012, **51**, 10760-10764.
18. J. Gu, Y. Yan, J. L. Young, K. X. Steirer, N. R. Neale and J. A. Turner, *Nat. Mater.*, 2016, **15**, 456-460.
19. F. Nandjou and S. Haussener, *J. Phys. D: Appl. Phys.*, 2017, **50**, 124002.
20. H. Kaneko, T. Minegishi and K. Domen, *Chem.*, 2018, **24**, 5697-5706.
21. L.-J. Guo, J.-W. Luo, T. He, S.-H. Wei and S.-S. Li, *Phys. Rev. Appl.*, 2018, **10**, 064059.
22. K. W. Frese, M. J. Madou and S. R. Morrison, *J. Phys. Chem.*, 1980, **84**, 3172-3178.
23. D. Bae, B. Seger, O. Hansen, P. C. K. Vesborg and I. Chorkendorff, *ChemElectroChem*, 2019, **6**, 106-109.
24. D. Bae, B. Seger, P. C. Vesborg, O. Hansen and I. Chorkendorff, *Chem. Soc. Rev.*, 2017, **46**, 1933-1954.
25. H. Gerischer, *J. Electroanalytical Chem. and Interfacial Electrochemistry*, 1975, **58**, 263-274.
26. S. Chen and L.-W. Wang, *Chem. Mater.*, 2012, **24**, 3659-3666.
27. S. Hu, M. R. Shaner, J. A. Beardslee, M. Lichterman, B. S. Brunschwig and N. S. Lewis, *Science*, 2014, **344**, 1005-1009.

28. S. W. Boettcher, E. L. Warren, M. C. Putnam, E. A. Santori, D. Turner-Evans, M. D. Kelzenberg, M. G. Walter, J. R. McKone, B. S. Brunschwig, H. A. Atwater and N. S. Lewis, *J. Am. Chem. Soc.*, 2011, **133**, 1216-1219.

29. H. J. Lewerenz, *J. Electrochem. Soc.*, 2014, **161**, H3117-H3129.

30. Y. Kuang, Q. Jia, G. Ma, T. Hisatomi, T. Minegishi, H. Nishiyama, M. Nakabayashi, N. Shibata, T. Yamada, A. Kudo and K. Domen, *Nat. Energ.*, 2016, **2**, 16191.

31. P. Dias, A. Vilanova, T. Lopes, L. Andrade and A. Mendes, *Nano Energ.*, 2016, **23**, 70-79.

32. N. P. Dasgupta, C. Liu, S. Andrews, F. B. Prinz and P. Yang, *J. Am. Chem. Soc.*, 2013, **135**, 12932-12935.

33. B. Fabre, G. Li, F. Gouttefangeas, L. Joanny and G. Loget, *Langmuir*, 2016, **32**, 11728-11735.

34. E. Kemppainen, A. Bodin, B. Sebok, T. Pedersen, B. Seger, B. Mei, D. Bae, P. C. K. Vesborg, J. Halme, O. Hansen, P. D. Lund and I. Chorkendorff, *Energ. Environ. Sci.*, 2015, **8**, 2991-2999.

35. C. U. Maier, M. Specht and G. Bilger, *Int. J. Hydrogen Energ.*, 1996, **21**, 859-864.

36. B. Zhou, X. Kong, S. Vanka, S. Chu, P. Ghamari, Y. Wang, N. Pant, I. Shih, H. Guo and Z. Mi, *Nat. Commun.*, 2018, **9**.

37. D. M. Andoshe, G. Jin, C.-S. Lee, C. Kim, K. C. Kwon, S. Choi, W. Sohn, C. W. Moon, S. H. Lee, J. M. Suh, S. Kang, J. Park, H. Heo, J. K. Kim, S. Han, M.-H. Jo and H. W. Jang, *Adv. Sus. Sys.*, 2018, **2**, 1700142.

38. R. Fan, S. Cheng, G. Huang, Y. Wang, Y. Zhang, S. Vanka, G. A. Botton, Z. Mi and M. Shen, *J. Mater. Chem. A*, 2019, **7**, 2200-2209.

39. E. L. Warren, J. R. McKone, H. A. Atwater, H. B. Gray and N. S. Lewis, *Energ. Environ. Sci.*, 2012, **5**, 9653.

40. M. T. McDowell, M. F. Lichterman, A. I. Carim, R. Liu, S. Hu, B. S. Brunschwig and N. S. Lewis, *ACS Appl. Mater. Interfaces*, 2015, **7**, 15189-15199.

41. R. Fan, W. Dong, L. Fang, F. Zheng and M. Shen, *J. Mater. Chem. A*, 2017, **5**, 18744-18751.

42. C. Ros, T. Andreu, M. D. Hernandez-Alonso, G. Penelas-Perez, J. Arbiol and J. R. Morante, *ACS Appl. Mater. Interfaces*, 2017, **9**, 21, 17932-17941.

43. R. Fan, W. Dong, L. Fang, F. Zheng, X. Su, S. Zou, J. Huang, X. Wang and M. Shen, *Appl. Phys. Lett.*, 2015, **106**, 013902.

44. B. Mei, B. Seger, T. Pedersen, M. Malizia, O. Hansen, I. Chorkendorff and P. C. K. Vesborg, *J. Phys. Chem. Lett.,* 2014, **5**, 1948-1952.

45. X. H. Zhou, R. Liu, K. Sun, D. Friedrich, M. T. McDowell, F. Yang, S. T. Omelchenko, F. H. Saadi, A. C. Nielander, S. Yalamanchili, K. M. Papadantonakis, B. S. Brunschwig and N. S. Lewis, *Energ. Environ. Sci.*, 2015, **8**, 2644-2649.

46. B. Seger, T. Pedersen, A. B. Laursen, P. C. Vesborg, O. Hansen and I. Chorkendorff, *J. Am. Chem. Soc.*, 2013, **135**, 1057-1064.

47. X. Chen and S. S. Mao, *Chem. Rev.*, 2007, **107**, 2891-2959.

48. M. G. Kibria, R. Qiao, W. Yang, I. Boukahil, X. Kong, F. A. Chowdhury, M. L. Trudeau, W. Ji, H. Guo, F. J. Himpsel, L. Vayssieres and Z. Mi, *Adv. Mater.*, 2016, **28**, 8388-8397.

49. X. Guan, F. A. Chowdhury, Y. Wang, N. Pant, S. Vanka, M. L. Trudeau, L. Guo, L. Vayssieres and Z. Mi, *ACS Energ. Lett.*, 2018, **3**, 2230−2231.

50. J. Su, Y. Wei and L. Vayssieres, *J. Phys. Chem. Lett.*, 2017, **8**, 5228-5238.

51. Y. He, S. Vanka, T. Gao, D. He, J. Espano, Y. Zhao, Q. Dong, C. Lang, Y. Wang, T. W. Hamann, Z. Mi and D. Wang, *Nano Res.*, 2019, DOI: 10.1007/s12274-019-2346-3.
52. Z. Yin, R. Fan, G. Huang and M. Shen, *Chem. Commun. (Camb)*, 2018, **54**, 543-546.
53. W. Vijselaar, R. M. Tiggelaar, H. Gardeniers and J. Huskens, *ACS Energ. Lett.*, 2018, **3**, 1086-1092.
54. T. D. Moustakas, *Phys. Status Solidi A*, 2013, **210**, 169-174.

Figure Captions

Figure 1. Schematic illustration of photoelectrochemical (PEC) photoelectrode and various surface protection schemes. (a) Illustration of a PEC device consisting of semiconductor photoelectrode and catalyst (pink color) on top. Photogenerated electrons (light cyan color spheres) and holes (red color spheres) are separated, and electrons are transferred to the catalyst active sites for proton reduction. (b) Illustration of the second generation of surface protection scheme which consists of semiconductor photoelectrode, conventional thick protection layer (green color) and catalyst. The device efficiency is often compromised with the use of such a surface protection, due to parasitic light absorption, reduced charge carrier separation and extraction, and/or undesirable charge carrier recombination (recombination centers denoted as light orange color), which leads to lower H_2 production (grey bubbles). (c) Illustration of the third generation of protection scheme, which consists of semiconductor photoelectrode, multi-functional protection layer (light blue color), and catalyst. The protection layer is inherently stable in electrolyte, which not only provides long-term stability but significantly enhances the light absorption, charge carrier separation, and extraction and further reduces surface recombination, thereby leading to enhanced efficiency. (d) Illustration of Pt/n^+-GaN nanowires on n^+-p Si photocathode as the third generation of surface protection scheme. The band-diagram at the bottom shows the unique advantage of negligible conduction band offset between n^+-GaN and n^+-Si, enabling efficient charge carrier extraction [9].

Figure 2: Structural and PEC characterization of n^+-GaN nanowires on n^+-p Si substrate. (a) 45° tilted SEM image of n^+-GaN nanowires on Si. (b) STEM image (HDAAF) of Pt

nanoparticles decorated n^+-GaN nanowire. Inset is the magnified HDAAF image of the highlighted box region (brown color) showing the distribution of Pt nanoparticles on the nanowire. (c) *J-V* curves of platinized n^+-GaN nanowires/n^+-*p* Si photocathode under AM 1.5G one-sun illumination (red curve) and dark (black curve) in 0.5M H_2SO_4. (d) ABPE of n^+-GaN nanowires/n^+-*p* Si photocathode under AM 1.5G one sun illumination.

Figure 3: Long term stability of platinized n^+-GaN/n^+-*p* Si photocathode. (a) Chronoamperometry long term stability measurements for platinized n^+-GaN nanowires/n^+-*p* Si photocathode at 0 V *vs.* RHE in 0.5M H_2SO_4 under AM 1.5G one sun illumination. (b) Stability results of the highlighted (brown dashed box) for 80-264 h runs (4th-12th regeneration cycles). (c) Stability results of the highlighted (green dashed box) for 1270-1539 h runs (59th-73rd regeneration cycles). (d) Stability results of the highlighted (red dashed box) for 2350-2640 h runs (113th-125th regeneration cycles). (e) LSV comparison between 0 h (red curves) and start of the 141st regeneration cycle (blue curves) under dark (dotted) and AM 1.5G one-sun illumination (solid) in 0.5M H_2SO_4. (f) V_{on} (versus RHE) variations at the start (purple) and end (red) of each regeneration cycle.

Figure 4: Structural characterization of platinized n^+-GaN/n^+-*p* Si photocathode after stability test. (a) 45° tilted SEM and (b) STEM of Pt-decorated n^+-GaN nanowire/n^+-*p* Si photocathode after 3,000 h stability experiment. Inset in (b): STEM HDAAF image showing fewer Pt nanoparticles non-uniformly distributed on the highlighted (brown dashed box) segment of n^+-GaN nanowire.

Figure 5: Faraday Efficiency of platinized n^+-GaN nanowires/n^+-p Si. H_2 generation for platinized n^+-GaN nanowires/n^+-p Si photocathode at 0 V *vs.* RHE under AM 1.5G one-sun illumination in 0.5M H_2SO_4 for (a) 0 h- 2 h and (b) 3000 h – 3002 h. Red dots represent the average amount of H_2 generated at various times, and the black dotted line is the theoretical amount of H_2 produced vs. time based on photocurrent. The sample area is 0.12 cm^2 which corresponds to a photocurrent density of ~38 mA/cm^2. (c) Total H_2 production in Lit/cm^2 at STP for Si based photocathodes with various protection schemes: MoS_2 [11], NiMo/NiSi [53], $Pt/TiO_2/Ti$ [42], Pt $NPs/TiO_2/Ti$ [10] and Pt/TiO_2 [23].

Figure 6: AFM analysis of planar n^+-GaN on n^+-p Si. Pristine sample without Pt nanoparticles (a) before reaction and (b) after 10 h stability test in 0.5M H_2SO_4 under AM 1.5G one-sun illumination.

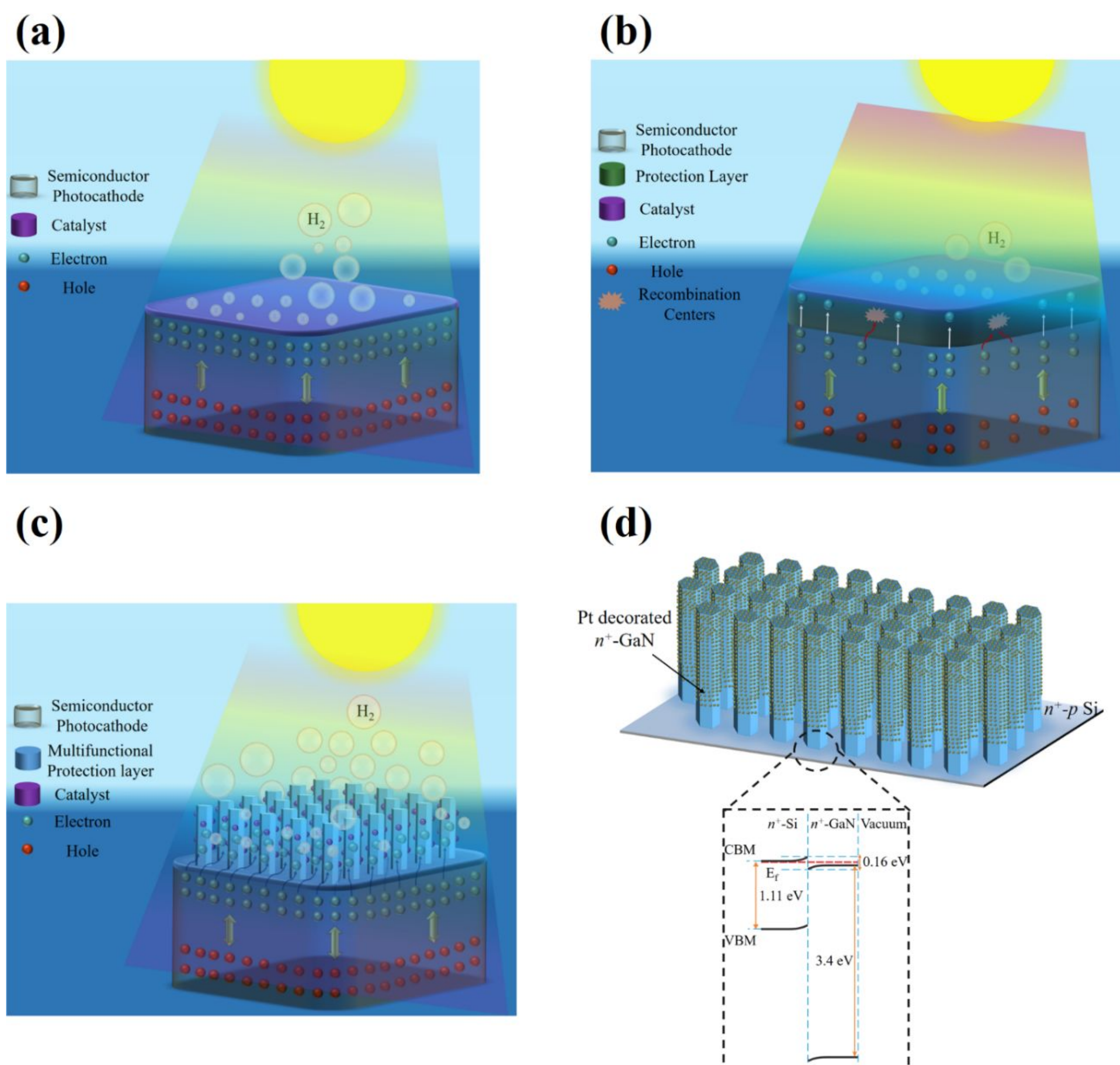

Figure 1. Schematic illustration of photoelectrochemical (PEC) photoelectrode and various surface protection schemes. (a) Illustration of a PEC device consisting of semiconductor photoelectrode and catalyst (pink color) on top. Photogenerated electrons (light cyan color spheres) and holes (red color spheres) are separated, and electrons are transferred to the catalyst active sites for proton reduction. (b) Illustration of the second generation of surface protection scheme which consists of semiconductor photoelectrode, conventional thick protection layer (green color) and catalyst. The device efficiency is often compromised with the use of such a surface protection, due to parasitic light absorption, reduced charge carrier separation and extraction, and/or undesirable charge carrier recombination (recombination centers denoted as light orange color), which leads to lower H_2 production (grey bubbles). (c) Illustration of the third generation of protection scheme, which consists of semiconductor photoelectrode, multi-functional protection layer (light blue color), and catalyst. The protection layer is inherently stable in electrolyte, which not only provides long-term stability but significantly enhances the light absorption, charge carrier separation, and extraction and further reduces surface recombination, thereby leading to enhanced efficiency. (d) Illustration of Pt/n^+-GaN nanowires on n^+-p Si photocathode as the third generation of surface protection scheme. The band-diagram at the bottom shows the unique advantage of negligible conduction band offset between n^+-GaN and n^+-Si, enabling efficient charge carrier extraction [9].

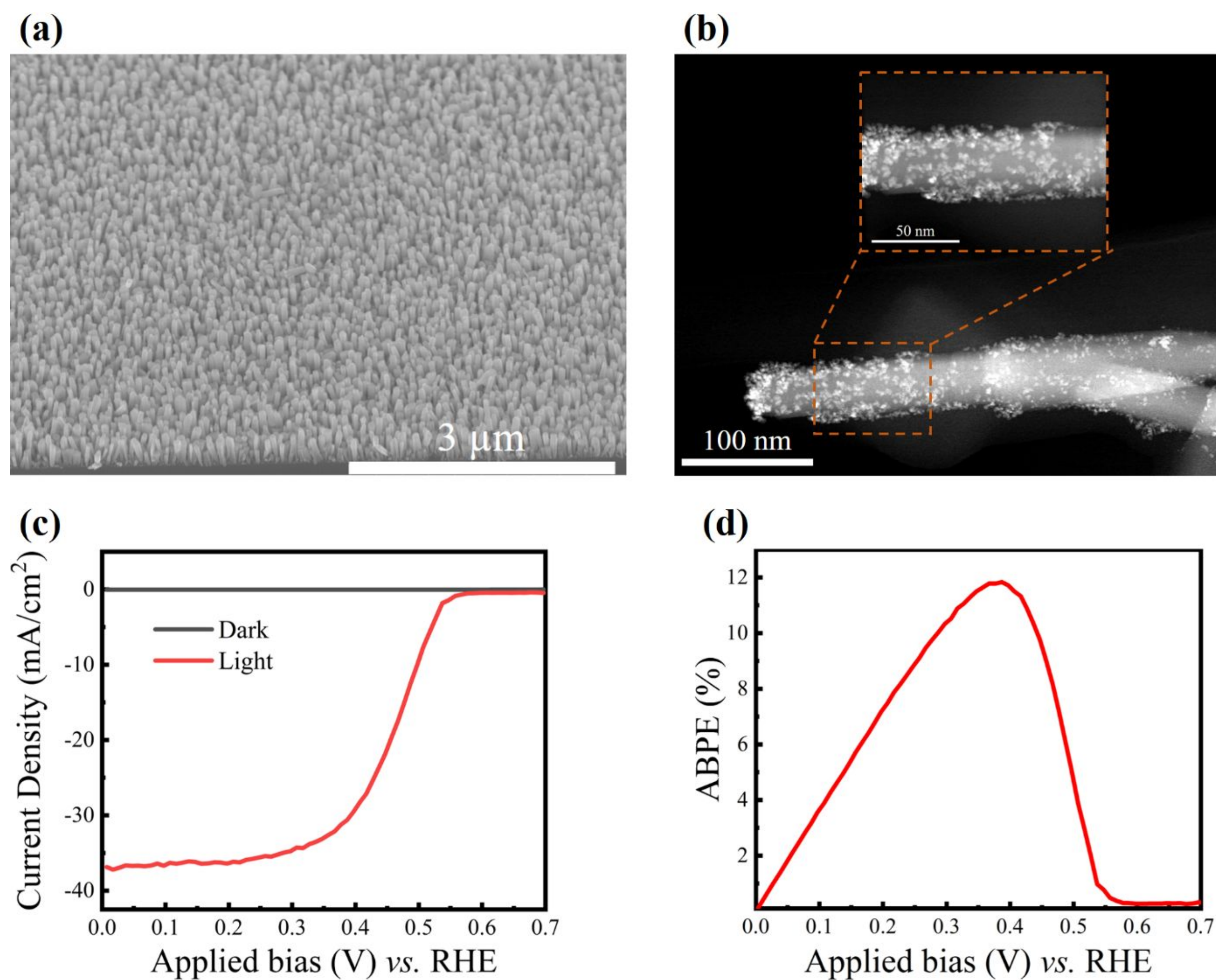

Figure 2: Structural and PEC characterization of n^+-GaN nanowires on n^+-p Si substrate. (a) 45° tilted SEM image of n^+-GaN nanowires on Si. (b) STEM image (HDAAF) of Pt nanoparticles decorated n^+-GaN nanowire. Inset is the magnified HDAAF image of the highlighted box region (brown color) showing the distribution of Pt nanoparticles on the nanowire. (c) *J-V* curves of platinized n^+-GaN nanowires/n^+-p Si photocathode under AM 1.5G one-sun illumination (red curve) and dark (black curve) in 0.5M H_2SO_4. (d) ABPE of n^+-GaN nanowires/n^+-p Si photocathode under AM 1.5G one sun illumination.

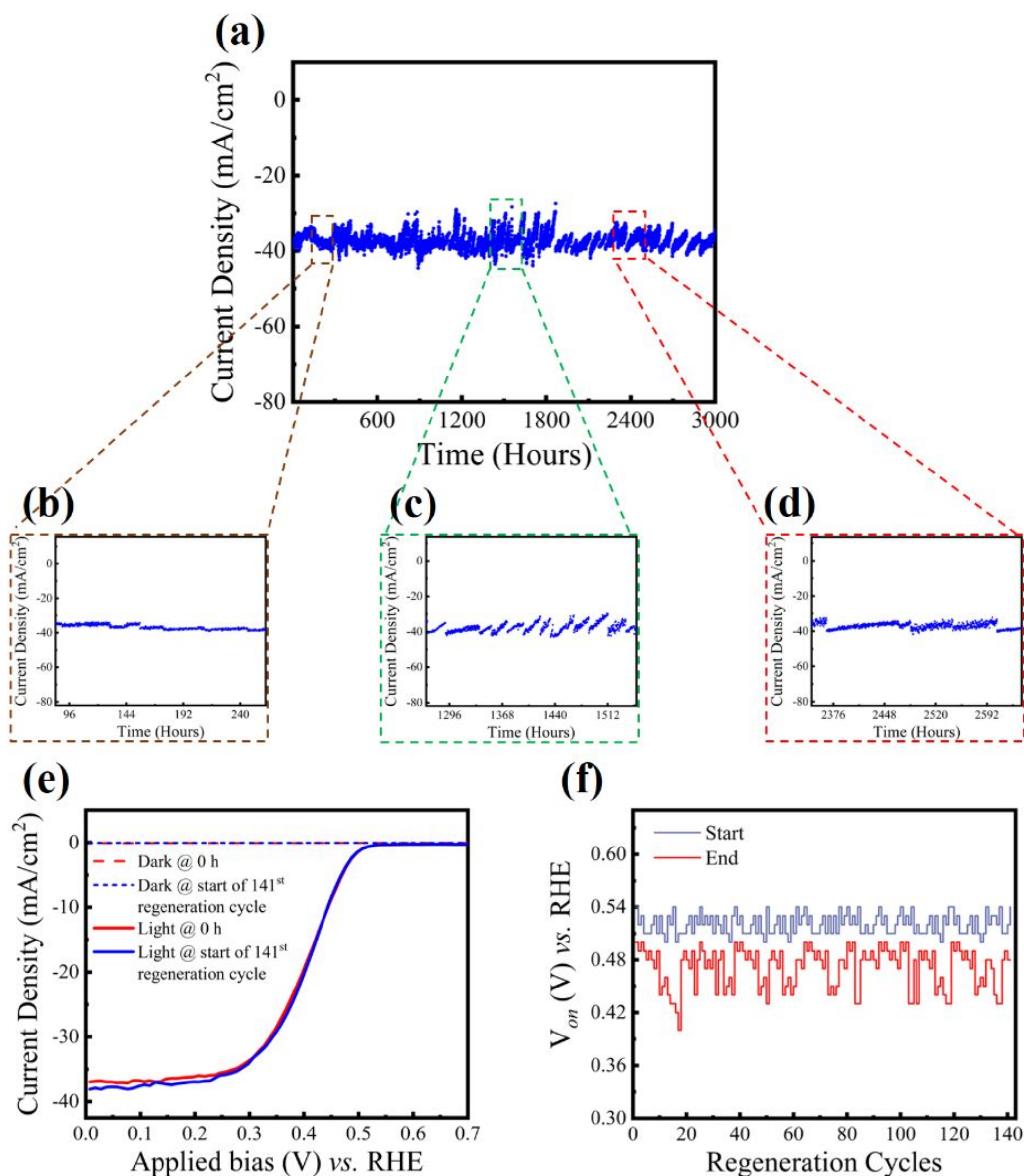

Figure 3: Long term stability of platinized n^+-GaN/n^+-p Si photocathode. (a) Chronoamperometry long term stability measurements for platinized n^+-GaN nanowires/n^+-p Si photocathode at 0 V *vs.* RHE in 0.5M H_2SO_4 under AM 1.5G one sun illumination. (b) Stability results of the highlighted (brown dashed box) for 80-264 h runs (4th-12th regeneration cycles). (c) Stability results of the highlighted (green dashed box) for 1270-1539 h runs (59th-73rd regeneration cycles). (d) Stability results of the highlighted (red dashed box) for 2350-2640 h runs (113th-125th regeneration cycles). (e) LSV comparison between 0 h (red curves) and start of the 141st regeneration cycle (blue curves) under dark (dotted) and AM 1.5G one-sun illumination (solid) in 0.5M H_2SO_4. (f) V_{on} (versus RHE) variations at the start (purple) and end (red) of each regeneration cycle.

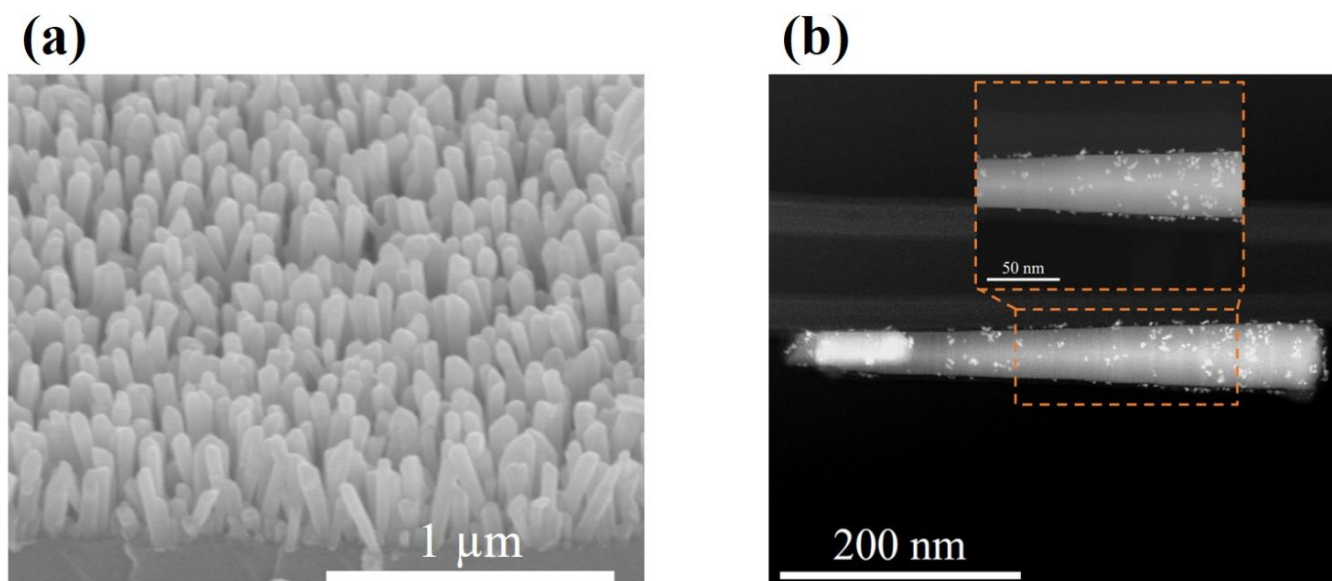

Figure 4: Structural characterization of platinized n^+-GaN/n^+-p Si photocathode after stability test. (a) 45° tilted SEM and (b) STEM of Pt-decorated n^+-GaN nanowire/n^+-p Si photocathode after 3,000 h stability experiment. Inset in (b): STEM HDAAF image showing fewer Pt nanoparticles non-uniformly distributed on the highlighted (brown dashed box) segment of n^+-GaN nanowire.

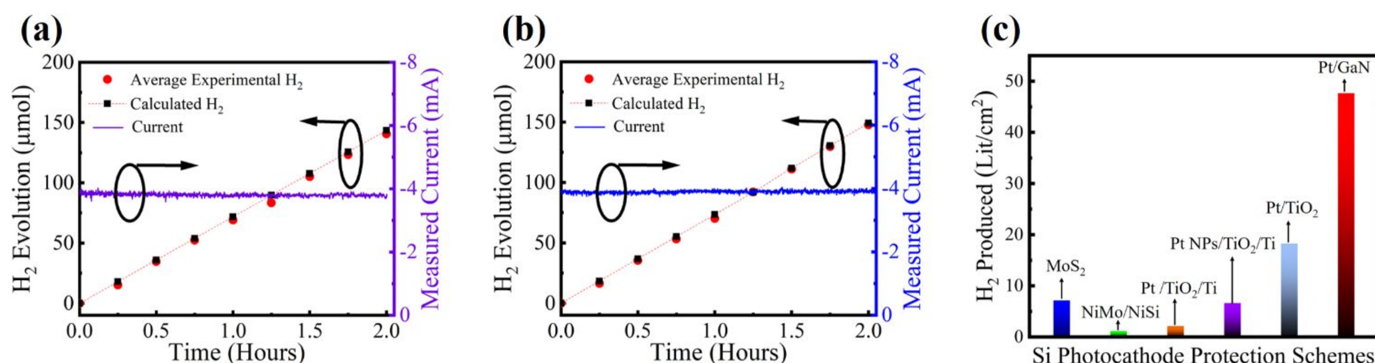

Figure 5: Faraday Efficiency of platinized n^+-GaN nanowires/n^+-p Si. H_2 generation for platinized n^+-GaN nanowires/n^+-p Si photocathode at 0 V *vs.* RHE under AM 1.5G one-sun illumination in 0.5M H_2SO_4 for (a) 0 h- 2 h and (b) 3000 h – 3002 h. Red dots represent the average amount of H_2 generated at various times, and the black dotted line is the theoretical amount of H_2 produced vs. time based on photocurrent. The sample area is 0.12 cm^2 which corresponds to a photocurrent density of ~38 mA/cm^2. (c) Total H_2 production in Lit/cm^2 at STP for Si based photocathodes with various protection schemes: MoS_2 [11], NiMo/NiSi [53], Pt/TiO_2/Ti [42], Pt NPs/TiO_2/Ti [10] and Pt/TiO_2 [23].

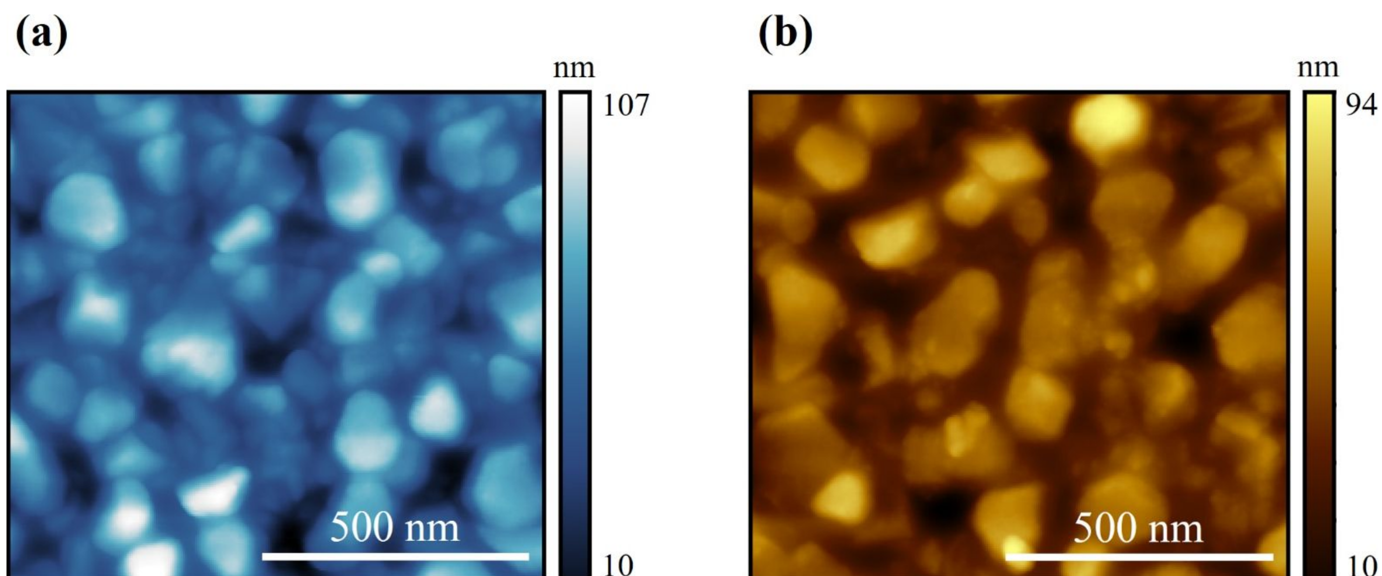

Figure 6: AFM analysis of planar n^+-GaN on n^+-p Si. Pristine sample without Pt nanoparticles (a) before reaction and (b) after 10 h stability test in 0.5M H_2SO_4 under AM 1.5G one-sun illumination.